RESEARCH PAPER

Advantages and limitations of an α-plasticity model for sand

Yifei Sun[1] · Wojciech Sumelka[2] · Yufeng Gao[3]

Abstract

The stress–strain response of sand was observed to depend on its material state, i.e., pressure and density. Successful modelling of such state-dependent response of sand relied on the correct representation of its state-dependent stress–dilatancy behaviour. In this study, an improved fractional-order (α) plasticity model for sands with a wide range of initial void ratios and pressures is proposed, based on a state-dependent fractional-order plastic flow rule and a modified yielding surface. Potential positive performances and negative limitations of the proposed approach in terms of the critical state of sand are discussed, based on the simulations of a series of drained and undrained triaxial tests of different sands. It can be found that unlike previous fractional models, the developed model can reasonably simulate the key features, e.g., strain softening/hardening, volumetric dilation/contraction, liquefaction, quasi-steady-state flow as well as steady-state flow, of sand for a wide range of initial states. However, due to typical forms of the critical-state lines being used, negative performances of the fractional approach could occur when simulating the undrained behaviour of very loose sand and the drained behaviour of very dense sand.

Keywords Fractional derivative · Liquefaction · Plasticity · Sand · State-dependent dilatancy

1 Introduction

The constitutive behaviour of sand, among other granular soils, is very complex and usually different from that of soft soils, e.g., clay. For clay, an associated plastic rule could provide accurate predictions of the stress–strain response [76]. However, for sand, an associated plastic flow rule would overpredict the volumetric dilation of sand samples [11, 26, 28, 37, 49–51]. In order to solve this

✉ Yufeng Gao
  yfgao66@163.com

  Yifei Sun
  sunny@hhu.edu.cn

  Wojciech Sumelka
  wojciech.sumelka@put.poznan.pl

1 Faculty of Civil and Environmental Engineering, Ruhr-Universität Bochum, 44801 Bochum, Germany

2 Institute of Structural Engineering, Poznan University of Technology, Piotrowo 5, 60-965 Poznan, Poland

3 Key Laboratory of Ministry of Education for Geomechanics and Embankment Engineering, College of Civil and Transportation Engineering, Hohai University, Nanjing 210098, China

problem, researchers often suggested to use an alternative stress–dilatancy equation, where the dilatancy angle was lower than the experimentally obtained friction angle [2, 65, 66, 78]. Improved performance of the model predictions was then reported. However, further researches on sands subjected to a wide range of initial void ratios and pressures revealed that the strength–deformation and stress–dilatancy behaviour of sand were highly dependent on its material state (pressure and density) [6, 7]. Constitutive models not considering such state dependence usually required different sets of model constants, in order to capture the constitutive behaviour of sand under different initial relative densities [5].

In the past decades, a substantial amount of effort had been devoted to the development of unified modelling of the stress–strain behaviour of sand [21, 36, 46, 47] and other granular soils [31, 34, 55, 68–72] with different initial states. It can be found that these approaches were developed by incorporating an empirical state parameter, for example, the state parameter ψ [6] and state pressure index I_p [67], into the friction angle at phase transformation state. A good agreement between the experimental results and model simulations was often reported. Nevertheless, the mathematical principles underlying the state-dependent

plastic flow were missing and open for discussion. Instead of simply using ψ or I_p, Sun et al. [59, 61] developed a rigorous mathematical elaboration of the state-dependent plastic flow rule for various granular soils, including sand, by using a stress-fractional operator as suggested in Sumelka [52] and Sumelka and Nowak [53]. Further validation against a series of experimental results showed that: the proposed stress–dilatancy equation can efficiently capture the state-dependent behaviour of sand with different initial material states. A state-dependent nonassociated α-plasticity model was then developed, based on a symmetric yielding surface [59]. However, due to the symmetry of the yielding surface, large elastic region would exist in the proposed model [14], which would result in the unrealistic prediction of the undrained behaviour of granular soils. Even though this aspect can sometimes be remedied by tuning the input model parameters, the model would be unable to capture the temporary peak or quasi-steady-state flow behaviour of sand before reaching the critical state.

This study aims to propose an improved α-plasticity model for sand with a wide range of initial densities and pressures, by using a state-dependent fractional-order plastic flow rule and a modified yielding surface. This paper is structured as follows: Sect. 2 presents the basic definitions of the critical state, Caputo's fractional derivative and constitutive relation for sand; Sect. 3 provides the derivations of the plastic loading, flow tensors and hardening modulus; Sect. 4 presents the detailed identification of model parameters; Sect. 5 validates the model against a series of triaxial test results of different sands with a variety of initial material states; Sect. 6 discusses the limitations of the proposed study; and Conclusions are drawn in Sect. 7. For the sake of simplicity, the study is limited to isotropic and homogeneous sands under triaxial loading, where the applied tensile stress and strain are considered as negative, while the compressive ones are positive.

2 Definitions

2.1 Critical state

All the model derivations and discussions in this study are within the framework of the critical state soil mechanics (CSSM) [48]. Therefore, upon sufficient shearing, sand would deform and finally reach the critical state, where infinite plastic flow with no change of the stress ratio and volumetric strain took place. Such kind of critical state can be defined by using two separate equations in the $p' - q$ and $e - p'$ planes, respectively. According to available experimental and numerical studies [4, 12, 39], the critical-state line in the $p' - q$ plane was linear and not influenced

by the breakage of sand particles. Similar to that of clay, it can be defined as:

$$q = M_c p' \tag{1}$$

where $p' = (\sigma'_1 + 2\sigma'_3)/3$ is the mean effective principal stress, while $q = \sigma'_1 - \sigma'_3$ is the deviator stress; σ'_1 and σ'_3 are the first and third effective principal stresses, respectively. To obtain the effective stress (σ'_i) from the total stress (σ_i), the Terzaghi's effective stress principle is applied, where $\sigma'_i = \sigma_i - u$; $i = 1, 2, 3$; u is the excess pore water pressure. Moreover, in Eq. (1), M_c is the critical-state stress ratio, which indicates the slope of the critical-state line in the $p' - q$ plane, as shown in Fig. 1. Before reaching critical state, there would be possibly two relative positions of the current stress point, i.e., above or below the critical-state line, as shown in Fig. 1. If the soil was sheared from the "wet" side, it would possibly stay below the critical-state line in the $p' - q$ plane, i.e., point B, until reaching the final critical state. If the soil was sheared from the "dry" side, it could be initially below the critical-state line in the $p' - q$ plane and then cross the critical-state line to stay at point A, until reaching the final critical state. Inspired by this laboratory observation, Sun et al. [61] suggested a unified equation to connect the current stress state with the critical-state line, such that:

$$q_c = q + M_c(p' - p'_c) \tag{2}$$

where q_c and p'_c are the critical-state stresses on the critical-state line, as shown in Fig. 1. It is easy to find that the solution of Eq. (2) depends on the determination of p'_c, which can be obtained by using the critical-state line in the $e - p'$ plane. Note that the critical-state line of sand in the $e - p'$ plane was totally different from that of clay. Due to significant breakage of sand particles during loading, the critical-state line in the $e - p'$ plane shifted with the varying void ratio (e) and pressure (p') [68, 69, 72, 79], as
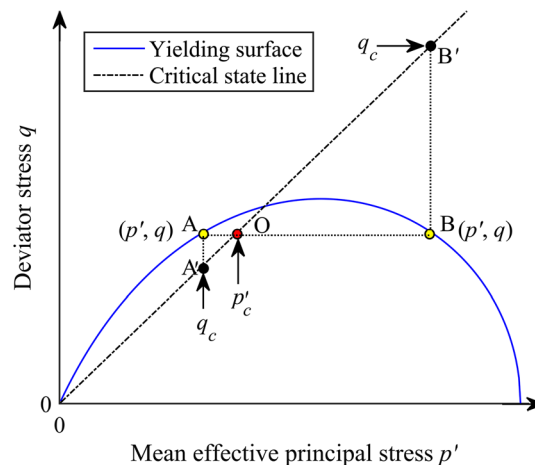

Fig. 1 Current stress state and critical-state line

evidenced in a number of studies [24]. In order to capture such unusual behaviour, a variety of nonlinear critical-state lines in the $e - p'$ plane had been proposed [10, 32, 33, 45]. However, the most commonly used one was suggested by Li and Wang [30] in the $e - (p'/p_a)^\xi$ plane, such that:

$$e = e_\Gamma - \lambda \left(\frac{p'}{p_a}\right)^\xi \tag{3}$$

where p_a = 100 kPa is the atmospheric pressure for normalisation; e_Γ, λ and ξ are the material constants describing the critical-state line in the $e - (p'/p_a)^\xi$ plane, as shown in Fig. 2. Specifically speaking, e_Γ and λ are the intercept (at $p' = 0$) and gradient of the critical-state line, respectively, while ξ is adaptive for a better linear correlation between e and $(p'/p_a)^\xi$. Then, rearranging Eq. (3), p'_c can be determined as [67]:

$$p'_c = p_a \left(\frac{e_\Gamma - e}{\lambda}\right)^{1/\xi}. \tag{4}$$

2.2 Caputo's fractional derivative

In the theory of fractional calculus, fractional derivative usually has two expressions: one is the left-sided derivative, the other is the right-sided one [44]. Following Caputo [1, 8, 9], they can be defined as:

$$_a D^\alpha_{\sigma'} g(\sigma') = \frac{1}{\Gamma(n-\alpha)} \int_a^{\sigma'} \frac{g^{(n)}(\chi)\mathrm{d}\chi}{(\sigma' - \chi)^{\alpha+1-n}}, \quad \sigma' > a \tag{5}$$

$$_{\sigma'} D^\alpha_a g(\sigma') = \frac{(-1)^n}{\Gamma(n-\alpha)} \int_{\sigma'}^a \frac{g^{(n)}(\chi)\mathrm{d}\chi}{(\chi - \sigma')^{\alpha+1-n}}, \quad a > \sigma' \tag{6}$$

where Eqs. (5) and (6) are the left-sided and right-sided fractional derivatives, respectively. $D (= \partial^\alpha/\partial\sigma'^\alpha)$ denotes
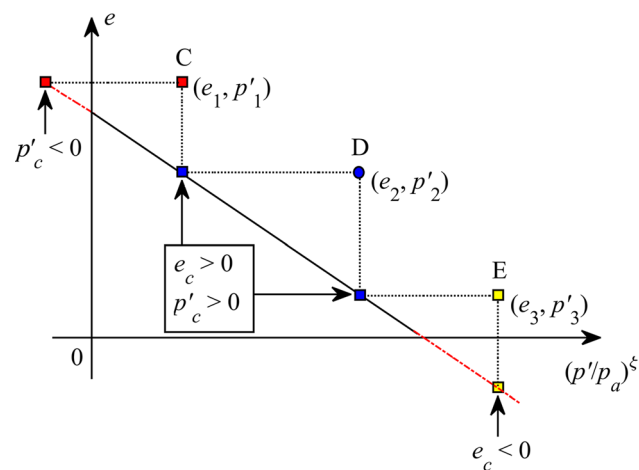

Fig. 2 Critical-state line and current state

the partial fractional derivative of function, g; $\alpha \in (n-1, n)$ is the fractional order [59], in which we restrict $n = 1$ or 2. As shown in Sun et al. [61], through strict mathematical derivation instead of empirical correlation, the state-dependent nonassociated plastic flow of granular soils can be captured by using the fractional derivatives. The fractional order, α, determines the (geometric) non-normality of a vector with respect to a surface; it also reflects the (physical) extent of state-dependent nonassociated plastic flow of granular soils in geomechanics. Moreover, χ is the independent variable for integration; $\Gamma(\chi) = \int_0^\infty \exp(-\tau)\tau^{\chi-1}\mathrm{d}\tau$ is the gamma function; σ' is the current stress in this study while a is the lower or upper limit for integration. In order to capture the state dependence of sand flow, $a = \sigma'_c$, where σ'_c denotes the critical-state stress in this study, because the final state a soil can reach is its critical state [48]. σ'_c should keep positive throughout the whole test. However, some previous studies [58] on fractional modelling only used the left-sided fractional derivative with $a = 0$, which, however, would make the model confronted with a dilemma: complex loading conditions cannot be easily captured [60], for example, (a) triaxial extension carried out by reducing σ'_1, where the current deviator stress would be less than zero; (b) loading after anisotropic consolidation, where the initial stress (i.e., a) could be no longer equal to zero; (c) stress reversal during cyclic loading, where a would be unrealistically larger than σ' in Eq. (5).

To solve this limitation and consider the different loading states indicated by points A and B in Fig. 1, a series of constitutive approaches using both the left-sided and right-sided fractional derivatives were then developed [59, 61]. The choice of Eqs. (5) or (6) depends on the relative location between the current stress state and the critical-state line. For example, if the current stress was at point A, then $p' < p'_c$ and $q > q_c$. Equation (5) would be used for calculating $_{p'} D^\alpha_{p'_c} g(p')$, whereas Eq. (6) would be used for calculating $_{q_c} D^\alpha_q g(q)$; or if the current stress was at point B where $p' > p'_c$ and $q < q_c$, Eq. (6) would be used for calculating $_{p'_c} D^\alpha_{p'} g(p')$, whereas Eq. (5) would be used for calculating $_q D^\alpha_{q_c} g(q)$. Note that even though left or right Caputo's fractional derivative is required due to the dependence of stress state, the final state-dependent stress–dilatancy equation is unique, as will be shown later.

2.3 Constitutive relation

The deformation of sand is considered to be consisted of two parts: elastic deformation and plastic deformation. Accordingly, the increment of the total strain ($\Delta\varepsilon$) can be decomposed as:

$$\Delta\boldsymbol{\varepsilon} = \Delta\boldsymbol{\varepsilon}^e + \Delta\boldsymbol{\varepsilon}^p \tag{7}$$

where $\boldsymbol{\varepsilon}^e = [\varepsilon_v^e, \varepsilon_s^e]^T$ is the elastic strain matrix, while $\boldsymbol{\varepsilon}^p = [\varepsilon_v^p, \varepsilon_s^p]^T$ is the plastic strain matrix, respectively. The superscripts, e and p, denote the elastic and plastic components, respectively, and ε_v and ε_s are the volumetric and generalised shear strains, respectively. Moreover, $\varepsilon_v = \varepsilon_1 + 2\varepsilon_3$ and $\varepsilon_s = 2(\varepsilon_1 - \varepsilon_3)/3$, in which ε_1 and ε_3 are the first and third principal strains, respectively. $\Delta\boldsymbol{\varepsilon}^e$ can be determined by using Hooke's law, such that:

$$\Delta\boldsymbol{\varepsilon}^e = \mathbf{C}^e \Delta\boldsymbol{\sigma}' \tag{8}$$

where $\boldsymbol{\sigma}' = [p', q]^T$ is the stress matrix. The elastic compliance $\mathbf{C}^e$ can be expressed as:

$$\mathbf{C}^e = \begin{bmatrix} 1/K \\ & 1/(3G) \end{bmatrix} \tag{9}$$

in which the shear modulus (G) and bulk modulus (K) can be defined as:

$$G = G_0 p_a \frac{(2.97 - e)^2}{1 + e} \sqrt{\frac{p'}{p_a}} \tag{10}$$

$$K = \frac{(2 + 2v)}{3(1 - 2v)} G \tag{11}$$

where G_0 is the elastic constant; v is the Poisson's ratio. Following Pastor et al. [41], the plastic strain matrix can be determined as:

$$\Delta\boldsymbol{\varepsilon}^p = \frac{1}{H} \mathbf{n}^T \mathbf{m} \Delta\boldsymbol{\sigma}' \tag{12}$$

where T denotes transpose, $\mathbf{m}$ and $\mathbf{n}$ are the plastic loading and flow matrices, respectively; H is the plastic modulus. Combining Eqs. (8) and (12), the elastoplastic constitutive relation for sand can be defined as:

$$\Delta\boldsymbol{\varepsilon}^e = \left[\mathbf{C}^e + \frac{1}{H} \mathbf{n}^T \mathbf{m} \right] \Delta\boldsymbol{\sigma}'. \tag{13}$$

3 Model development

3.1 Plastic loading tensor

The plastic loading matrix defines the loading direction of sand. During undrained loading condition, the loading path in the $p' - q$ plane is approximately equivalent to the yielding surface [46]. Therefore, the original MCC yielding surface used by Sun et al. [61] may not well capture the undrained behaviour of sand. For example, specimens with low initial density would experience low elastic strain, and quasi-steady-state flow with a temporary stress peak
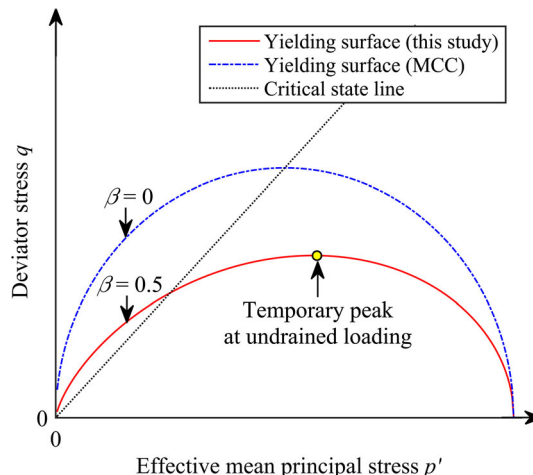

Fig. 3 Comparison between MCC and modified yielding surfaces

(Fig. 3) before reaching critical state. To consider such behaviour of sand, a modified yielding surface with shrunken size (reduced elastic region) should be used. Therefore, a modified yielding surface as shown in Fig. 3 is suggested in this study:

$$f = q^2 + M_c^2 p'^2 - M_c^2 p'^{1+\beta} p_0'^{1-\beta} \tag{14}$$

where p_0' represents the size of the yielding surface; similar to Yao et al. [74, 77], $\beta \in [0, 1]$ is a material constant, which can be determined by fitting the undrained triaxial loading path of loose sand specimen. It should be noted that as β increases from 0 to 1, the yielding surface shrinks more, where less elastic region exists. Then, the plastic loading matrix can be defined as:

$$\mathbf{m} = \frac{1}{\sqrt{1 + d_f^2}} [d_f, 1]^T \tag{15}$$

where d_f can be determined by:

$$d_f = \frac{D^1 f(p')}{D^1 f(q)} = \frac{(1 - \beta) M_c^2 - (1 + \beta) \eta^2}{2\eta} \tag{16}$$

It can be found from Eq. (16) that: when $\beta = 0$, the proposed plastic loading matrix reduces to the classical modified Cam-clay (MCC) model. However, when $\beta = 1$, it reduces to the purely shear-induced plastic loading case with $f = q - \eta p'$; this yielding function was often used for granular soils [13, 29].

3.2 Plastic flow tensor

According to available experimental results [6, 7, 64, 70], the plastic flow or stress–dilatancy of granular soils, including sand, exhibited highly dependence on the material state. To capture such state-dependent plastic flow of granular soil, various state-dependent stress–dilatancy

equations have been developed by using empirical state parameters [10, 16, 17, 25, 31, 41, 57]. Without using predefined empirical state parameters, Sun et al. [61] theoretically developed a state-dependent stress–dilatancy equation, by conducting fractional derivatives of the MCC yielding surface. To keep consistent with the previous study, $\beta = 0$ is used when deriving the plastic flow matrix. Further substituting Eq. (14) into Eqs. (5) and (6), one has:

$$
d_g = -\frac{p' D^{\alpha}_{p'_c} f}{q_c D^{\alpha}_{q} f} = -\frac{p'_c D^{\alpha}_{p'} f}{q D^{\alpha}_{q_c} f}
$$
$$
= M_c^{1+\alpha} \frac{(p' - p'_c) + (2 - \alpha)(p'_c - p'_0/2)}{(q - q_c) + (2 - \alpha) q_c}
\tag{17}
$$

As can be observed, if $\alpha = 1$, Eq. (17) would reduce to the traditional MCC stress–dilatancy equation with no state dependence. However, if α = non-integer, a clear state dependence can be achieved via $p' - p'_c$ and $q - q_c$, which are the horizontal and vertical distances from the current stress point to the critical-state line. Thus, as α deviates from unit, the extent of state dependence increases [61]. Moreover, with the increase of α, a higher volumetric dilation could be also observed. For more details of the effect on stress–dilatancy, one can refer to Sun et al. [59, 61]. In triaxial loading condition, the plastic flow matrix can be defined as:

$$
\mathbf{n} = \frac{1}{\sqrt{1 + d_g^2}} [d_g, 1]^T.
\tag{18}
$$

3.3 Hardening modulus

Sand specimens tested from the "wet" side of the critical-state line would exhibit strain hardening. In contrast, strain softening behaviour would be observed in sand specimens tested from the "dry" side of the critical-state line. The transition from hardening to softening also depends on material state [18, 19, 22]. To correctly capture such hardening/softening behaviour of sand, a reasonable state-dependent hardening modulus should be required. In this study, the hardening modulus developed by Li and Dafalias [29] is adopted, such that

$$
H = h_0 G \left\{ \frac{M_c}{\eta} - \exp \left[\vartheta (e - e_{\Gamma} + \lambda (p'/p_a)^{\xi}) \right] \right\}
\tag{19}
$$

where $h_0 = h_1 - h_2 e$, in which h_1 and h_2 are the hardening parameters; and ϑ is a material constant. Note that by using Eq. (19) as hardening modulus, pure compression-induced soil hardening cannot be considered, which would result in the inability of the model in predicting pure compressive deformation. But, in engineering practice, soils are rarely subjected to pure compressive load only. For isotropic or oedometer compression of soils, specific modelling

approaches, using either empirical correlation [42, 43] or theoretical derivation [38, 50], were usually reported, which, however, is not within the scope of this study.

4 Identification of model parameters

It can be found that there are eleven parameters in the developed α-plasticity model: M_c, e_{Γ}, λ, ξ, β, α, n, h_1, h_2, G_0 and v, which can be all identified from traditional triaxial test results. All the model parameters are dimensionless.

The critical-state stress ratio, M_c, can be determined by measuring the gradient of the critical-state line in the $p' - q$ plane. The rest three critical-state parameters, e_{Γ}, λ and ξ, can be identified by fitting the critical-state data points in the $e - p'$ plane [30], through least square method.

The shape parameter, β, can be determined by fitting the undrained stress path of the soil at its loose state [25].

The fractional order, α, can be obtained at the phase transformation state where $d_g = 0$, such that:

$$
\alpha = \frac{2 M_c^2 p_a [(e_{\Gamma} - e_{pt})/\lambda]^{1/\xi} - 2 \eta_{pt}^2 p'_{pt}}{2 M_c^2 p_a [(e_{\Gamma} - e_{pt})/\lambda]^{1/\xi} - M_c^2 p'_{pt} - \eta_{pt}^2 p'_{pt}}
\tag{20}
$$

where e_{pt}, p'_{pt} and η_{pt} are the void ratio, effective mean principal stress and stress ratio, respectively, at phase transformation state.

The peak-state parameter, ϑ, defines the state dependence of the peak stress ratio during drained loading, where $H = 0$. Therefore, it can be obtained by:

$$
\vartheta = \frac{\ln(M_c/\eta_f)}{e_f - e_{\Gamma} + \lambda (p'_f/p_a)^{\xi}}
\tag{21}
$$

where e_f, p'_f and η_f are the void ratio, effective mean principal stress and stress ratio, respectively, at peak failure state.

The two hardening parameters, h_1 and h_2, define the hardening behaviour of soil, which can be determined by fitting the $\varepsilon_s - q$ relationship [29, 63]. It can be also determined from the drained triaxial test where $\dot{p}' = \dot{q}/3$. Assuming the elastic strain is small and substituting $\dot{p}' = \dot{q}/3$ into Eq. (13), one has:

$$
h_0 = \frac{\eta(1 + d_f/3)\dot{q}/\dot{\varepsilon}_s/\sqrt{1 + d_f^2}/\sqrt{1 + d_g^2}}{G \left\{ M_c - \eta \exp \left[n(e - e_{\Gamma} + \lambda(p'/p_a)^{\xi}) \right] \right\}}
\tag{22}
$$

Then, h_0 can be calibrated from the $\varepsilon_s - q$ relationship, where h_1 and h_2 can be further identified by fitting the relationship between e and h_0, as clearly shown in Taiebat et al. [63].

The two elastic constants, G_0 and v, can be obtained from the $\varepsilon_s - q$ relationship at the initial loading stage ($\varepsilon_s \approx \varepsilon_s^e$) [61], where G_0 can be obtained by rearranging Eqs. (8)–(10):

$$G_0 \approx \frac{(1+e)G}{(2.97-e)^2\sqrt{p'p_a}} \tag{23}$$

$$v \approx \frac{3\varepsilon_s - 2\varepsilon_v}{6\varepsilon_s + 2\varepsilon_v}. \tag{24}$$

5 Model validation

In this section, the proposed model will be validated against a series of drained and undrained triaxial test results of six different sands, including Hostun RF sand [40] (Figs. 4, 5), Hostun III sand [15] (Fig. 6), Firoozkuh sand [3] (Fig. 7), Fuji River sand [20] (Figs. 8, 9), Toyoura sand [64] (Figs. 10, 13) and Sacramento River sand [27] (Figs. 14, 16). It is noted that test results are represented in coloured data points, while model predictions are shown by black solid lines. Detailed values of each model parameter are shown in Table 1. Note that as analytical solutions of the fractional derivative with respect to the assumed yielding function have been obtained, the subsequent numerical computation of the model would not involve any resolution of the fractional derivative. Therefore, the
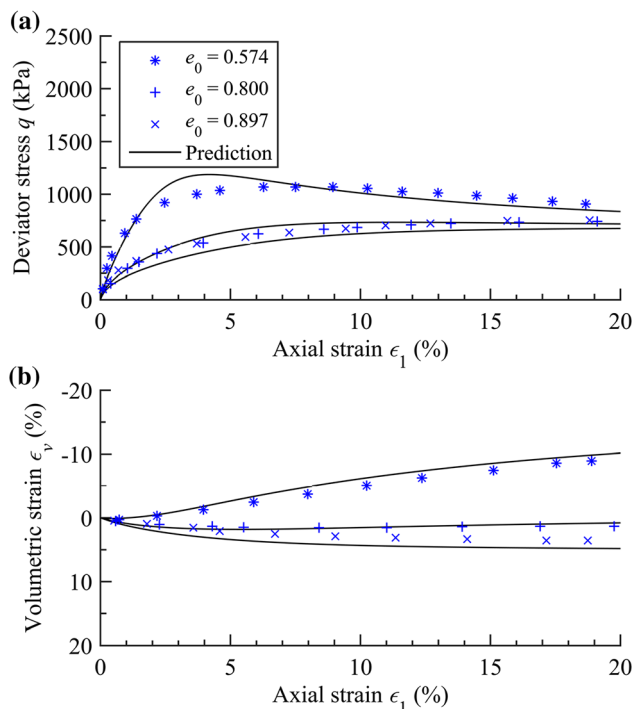
Fig. 4 Drained response of Hostun RF sand: model predictions versus test results [40]
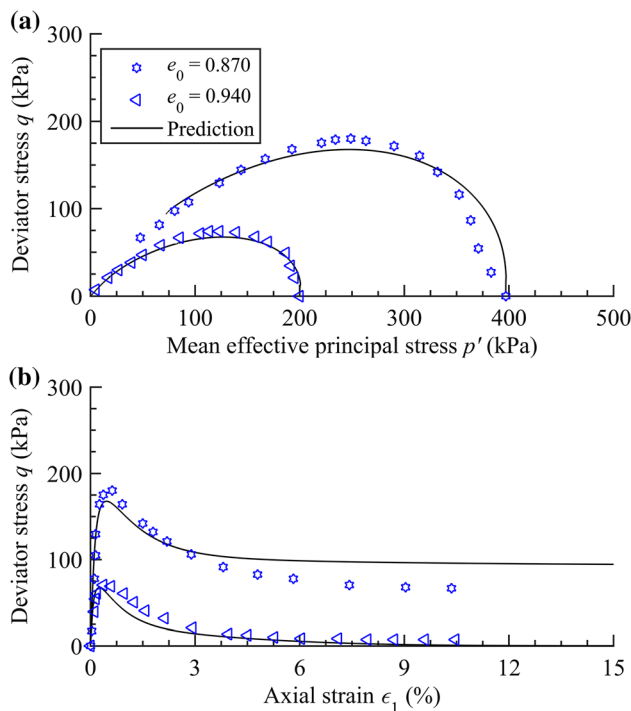
Fig. 5 Undrained response of Hostun RF sand: model predictions versus test results [40]
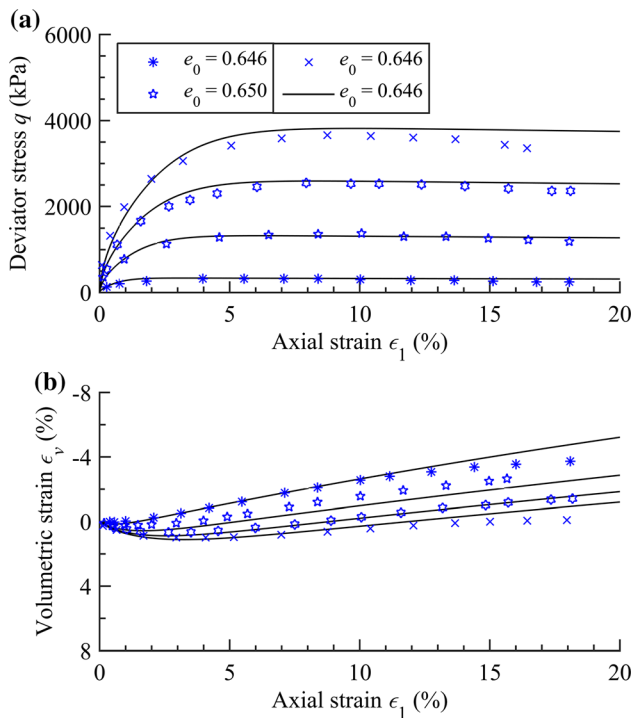
Fig. 6 Drained response of Hostun III sand: model predictions versus test results [15]

computational overhead of this approach should be equivalent to the traditional approaches using integer-order derivative.
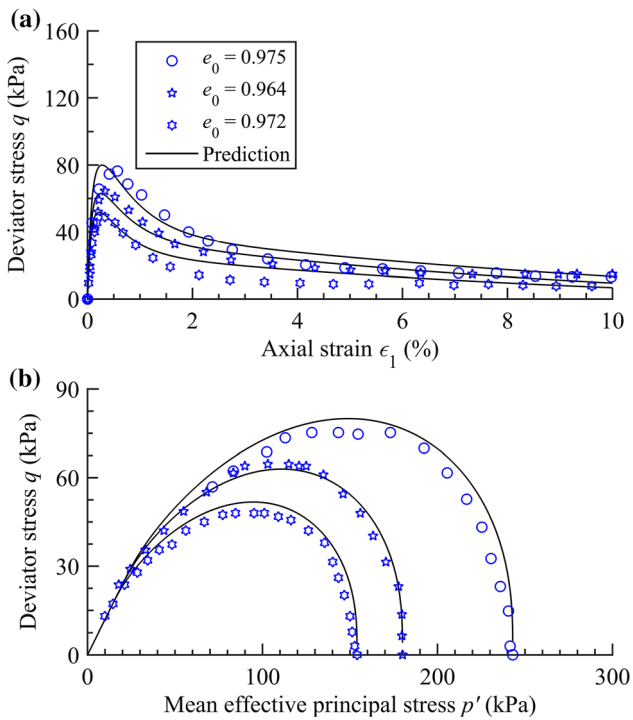
Fig. 7 Undrained response of Firoozkuh sand: model predictions versus test results [3]
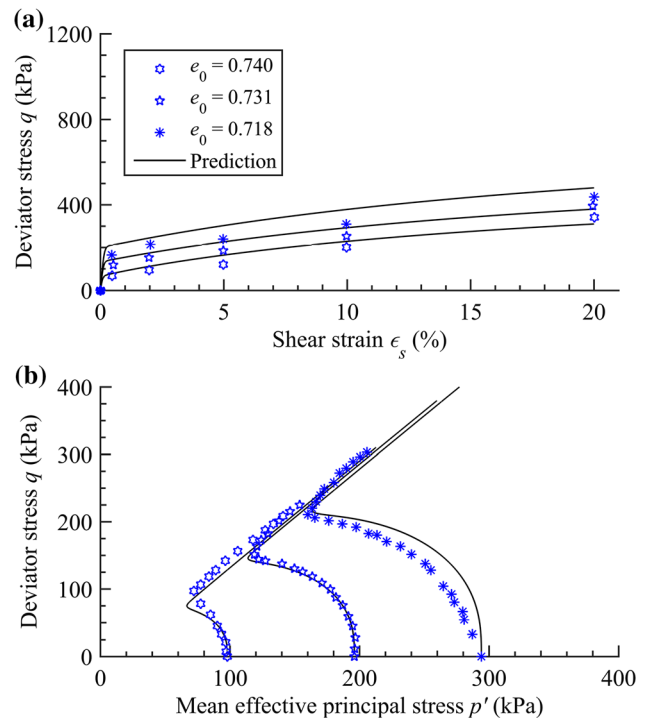

Fig. 8 Drained response of Fuji River sand: model predictions versus test results [20]
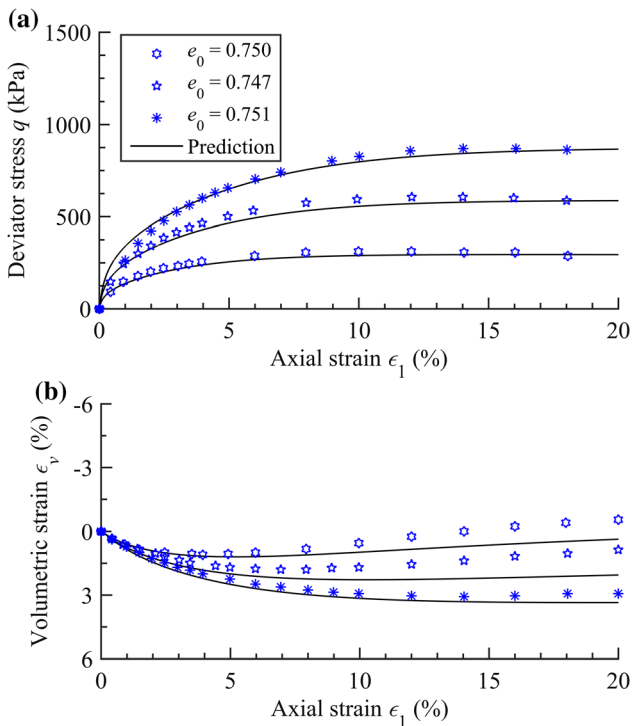

Fig. 9 Undrained response of Fuji River sand: model predictions versus test results [20]
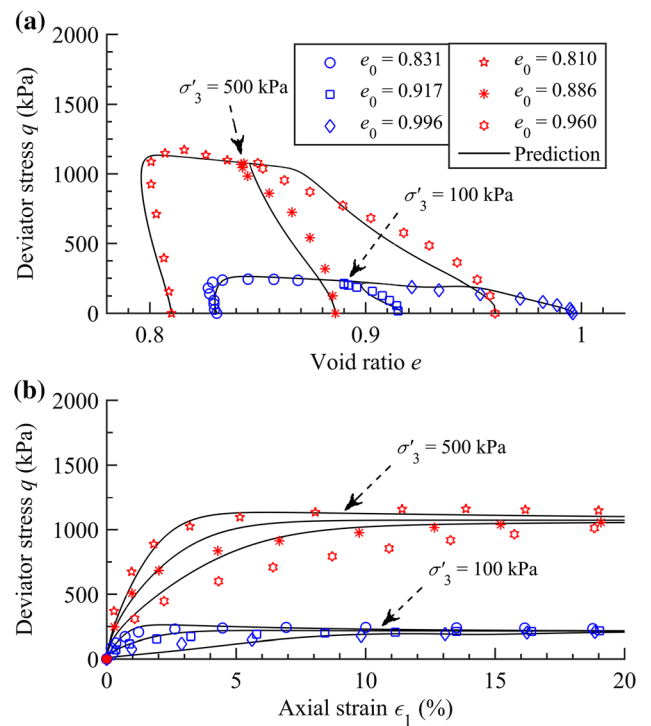

Fig. 10 Drained response of Toyoura sand: model predictions versus test results [64]

Figures 4 and 5 show the model simulations of the drained and undrained triaxial tests of Hostun RF sand

carried out by Meghachou [40]. It was found that the sand mainly consisted of angular quartz particles, with a median

Table 1 Model parameters

Soil type	e_Γ	λ	ξ	M_c	α	ϑ	β	h_1	h_2	G_0	v
Hostun RF sand [40]	0.955	0.094	0.3	1.30	1.050	1.5	0.85	2	2	80	0.04
Hostun III sand [15]	0.953	0.010	0.7	1.40	1.002	0.45	0.84	0.9	0.9	290	0.10
Firoozkuh sand [3]	0.923	0.057	0.5	1.22	1.000	1.2	0.75	3	3	100	0.11
Fuji River sand [20]	0.810	0.033	0.7	1.49	1.060	0.5	0.30	1.5	1.5	90	0.30
Toyoura sand [64]	0.934	0.019	0.7	1.25	1.10	1.1	0.80	3.5	3.5	125	0.05
Sacramento River sand [27]	0.960	0.028	0.7	1.35	1.040	0.9	0.65	6	6.05	100	0.20

particle size (d_{50}) equal to 0.35–0.38 mm and a coefficient of uniformity (C_u) equal to 1.8. The maximum (e_{max}) and minimum (e_{min}) void ratios were tested to be 1 and 0.656, respectively. All the specimens were prepared by moist-tamping technique in laboratory. A wide range of the initial densities from dense state ($e_0 = 0.574$) to medium dense ($e_0 = 0.8$) and loose states ($e_0 = 0.897$) were used for conducting the drained triaxial tests at an initial confining pressure σ'_3 of 300 kPa. As shown in Fig. 4, the developed α-plasticity model can well capture the hardening and softening behaviour of Hostun RF sand. For dense and medium dense sands, the specimen volume initially contracted, and then continuously dilated; while for loose sand, a general volumetric contraction is observed, which can be all accurately predicted by the proposed model. Figure 5 shows the model predictions of the undrained test results of Hostun RF sand with two different e_0 (= 0.94, 0.87) and σ'_3 (= 200 kPa, 397 kPa). As observed, the proposed model can also reasonably characterise the undrained behaviour of Hostun RF sand. With the increase of shear strain, the predicted deviator stress of Hostun RF sand increases and then decreases rapidly towards a state of liquefaction instability, which matches well with the corresponding test results.

Figure 6 presents the model simulations of the drained triaxial behaviour of Hostun III sand [15] under a wide range of pressures (100–1200 kPa). The sand was reported to consist of sub-angular particles with a d_{50} of 0.307, C_u of 2.3, e_{max} of 0.953 and e_{min} of 0.612. The e_0 of 0.646, 0.646, 0.650 and 0.646 were used for tests carried out at σ'_3 of 100 kPa, 400 kPa, 800 kPa and 1200 kPa, respectively. It can be found that all specimens were tested under medium to dense states, and thus exhibited volumetric dilation at the end of the test. Comparisons between the model simulations and the corresponding test results show that: the model can appropriately predict the stress–strain response of Hostun III sand, where strain hardening/softening and volumetric dilation with varying degrees can be all captured.

Figure 7 shows the model predictions of the undrained liquefaction behaviour of Firoozkuh sand [3] under

different initial loading pressures. The Firoozkuh sand was a crusher-run sandy soil that consisted of sub-angular quartz particles. It had a d_{50} of 0.26, C_u of 1.9, e_{max} of 0.943 and e_{min} of 0.568. All the specimens were prepared by using moist-tamping method. Three different σ'_3 of 243 kPa, 180 kPa and 154 kPa, with the corresponding e_0 of 0.975, 0.964 and 0.972, were used, respectively, for model simulations. As the specimens were initially at loose state, it can be found that they all liquefied and become instable at the end of the tests. The proposed model can accurately capture such liquefaction instability behaviour of Firoozkuh sand.

Figures 8 and 9 show the model simulations of the drained and undrained triaxial behaviour of Fuji River sand [20]. The sand mainly consisted of sub-angular particles with a d_{50} of 0.22 mm, C_u of 2.21, e_{max} of 0.99 and e_{min} of 0.55. All the specimens were prepared by using pluviation method. For drained tests, the e_0 of 0.750, 0.747 and 0.751 with the respective σ'_3 of 98 kPa, 196 kPa and 294 kPa were used to carried out, whereas for undrained tests, the e_0 of 0.740, 0.731 and 0.718 with the respective σ'_3 of 98 kPa, 196 kPa and 294 kPa were used. It can be found that both the drained and undrained behaviour of Fuji River sand can be well predicted by using the α-plasticity model. Particularly, the model predictions exhibit an accurate match with the strain hardening data during drained loading. In addition, all the specimens underwent steady-state flow at the end of the undrained tests, which can be also reasonably captured by the model.

Figures 10, 11, 12 and 13 show the model predictions of the drained and undrained triaxial behaviour of Toyoura sand [64] with a wide range of initial void ratios and pressures. It was found that the sand mainly consisted of sub-round/sub-angular particles with a d_{50} of 0.17 mm, C_u of 1.7, e_{max} of 0.977 and e_{min} of 0.597. The moist placement method was used for specimen preparation. For drained tests, two different confining pressures were used: $\sigma'_3 = 100$ kPa for the corresponding e_0 of 0.831, 0.917 and 0.996; $\sigma'_3 = 500$ kPa for the corresponding e_0 of 0.810, 0.886 and 0.960. For undrained tests, three different void ratios representing the dense ($e_0 = 0.735$), medium dense
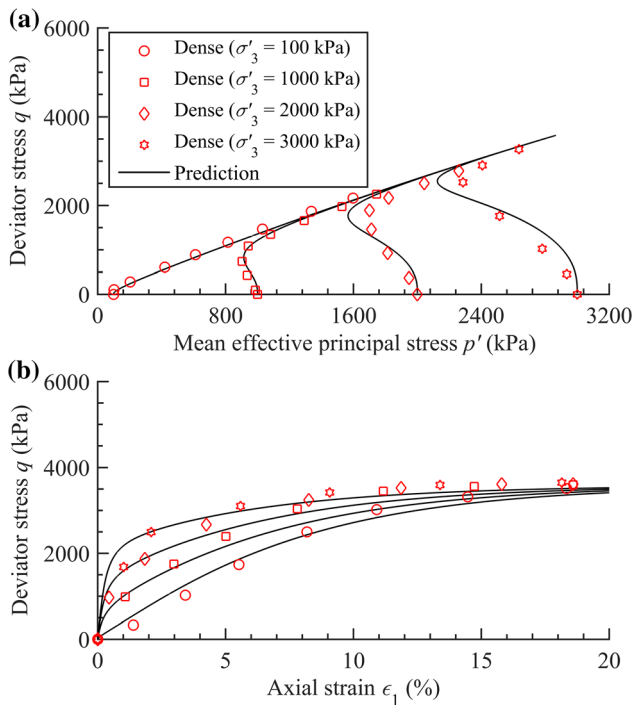
Fig. 11 Undrained response of dense Toyoura sand: model predictions versus test results [64]
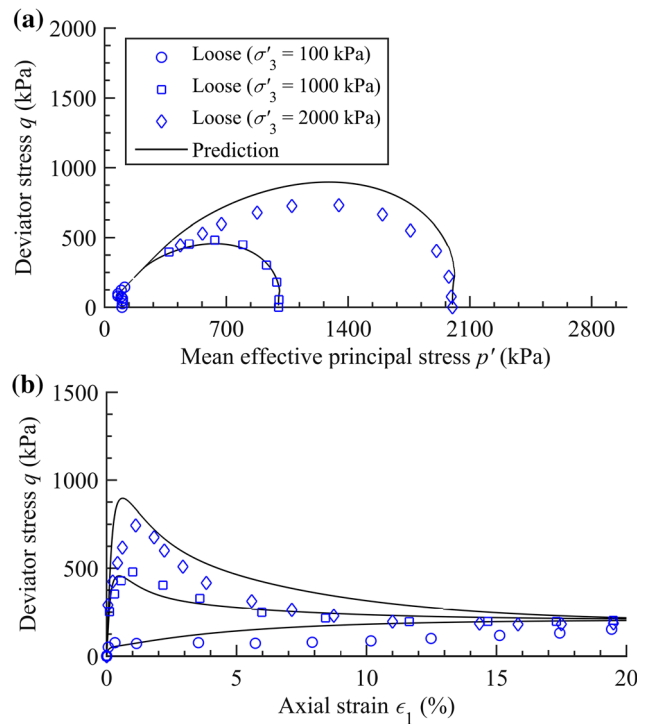

Fig. 12 Undrained response of medium dense Toyoura sand: model predictions versus test results [64]

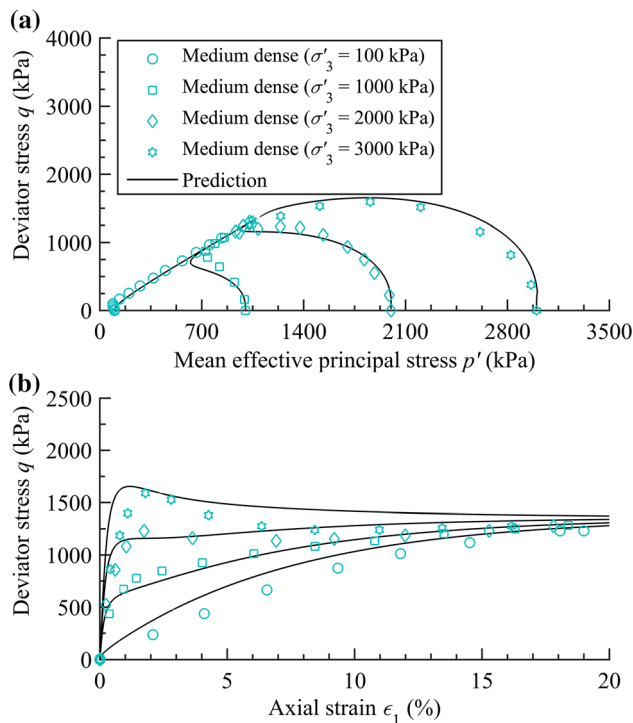Fig. 13 Undrained response of loose Toyoura sand: model predictions versus test results [64]

($e_0 = 0.833$) and loose ($e_0 = 0.907$) states of Toyoura sand were used. As can be observed in Fig. 10, the proposed model simulates well the drained triaxial behaviour of

Toyoura sand under different loading pressures. Irrespective of the applied confining pressure, specimens with low void ratios ($e_0 = 0.810, 0.831$) all exhibited some level of volumetric dilation, while those with relatively higher e_0 only experienced volumetric contraction throughout the entire tests. Moreover, Figs. 11, 12 and 13 show the model predictions of the undrained triaxial behaviour of Toyoura sand. For dense specimens shown in Fig. 11, the deviator stress increased continuously with the increase of shear strain, whereas the mean effective principal stress firstly decreased and then increased until reaching critical state, which can be well predicted by using the α-plasticity model. For medium dense specimens shown in Fig. 12, test results under σ'_3 of 100 kPa and 1000 kPa exhibited a continuous increase of the deviator stress with the increase of shear strain, while a temporary peak followed a slight decrease of the deviator stress can be observed in test under $\sigma'_3 = 2000$ kPa. For test result obtained under $\sigma'_3 = 3000$ kPa, an initial increase followed by a decrease of the deviator stress was reported. Irrespective of the loading pressures, all the tested specimens reached the critical state under sufficient triaxial shearing. These features can be all addressed appropriately by the proposed model. For loose specimens shown in Fig. 13, liquefaction instability was observed in tests under $\sigma'_3 = 1000$ kPa, 2000 kPa, whereas an increase of the deviator stress was
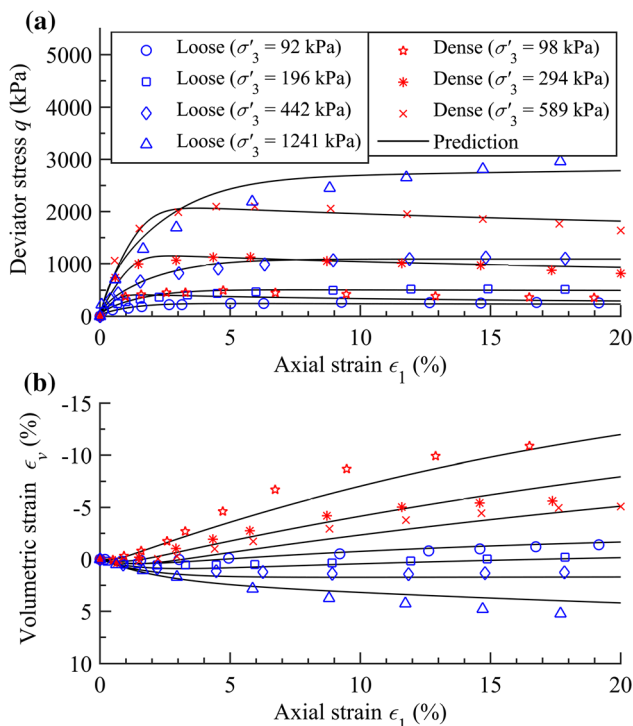
Fig. 14 Drained response of Sacramento River sand: model predictions versus test results [27]
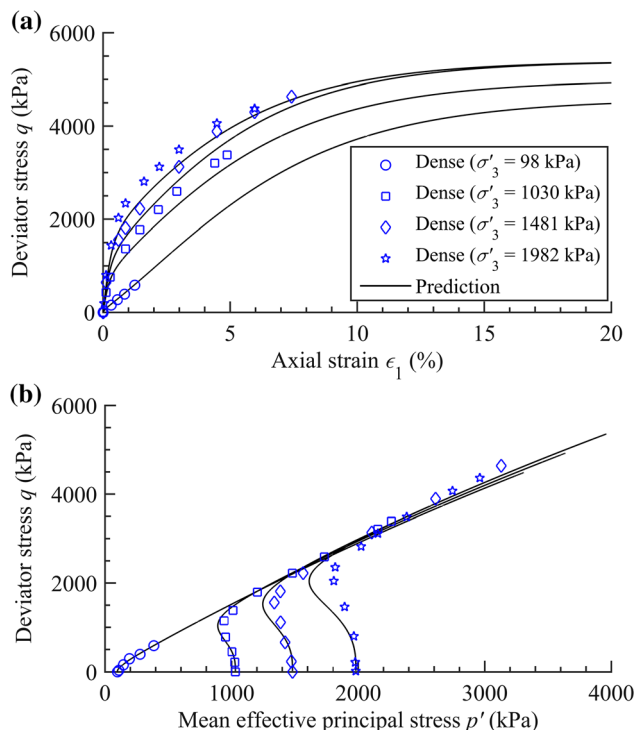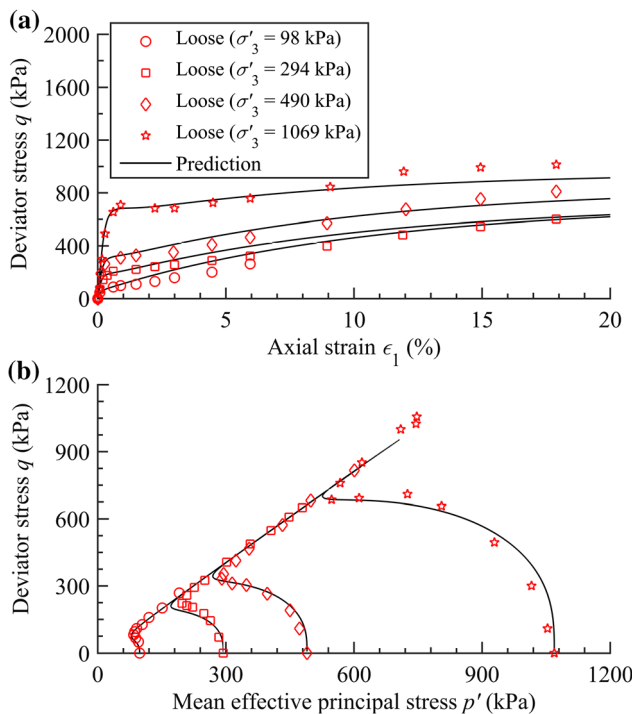

Fig. 15 Undrained response of loose Sacramento River sand: model predictions versus test results [27]

reported in test under $\sigma'_3 = 100$ kPa. These characteristics can be also well captured by the developed model.

Fig. 16 Undrained response of dense Sacramento River sand: model predictions versus test results [27]

Figures 14, 15 and 16 show the model simulations of the drained and undrained triaxial test results of dense and loose Sacramento River sand [27]. The sand was reported to contain fine and uniformly graded quartz particles with sub-rounded shape. It had a minimum particle size (d_m) of 0.149 mm, maximum particle size (d_M) of 0.297, e_{max} of 1.03 and e_{min} of 0.61. For drained tests, the e_0 of 0.87, 0.87, 0.87 and 0.85 are used for simulating loose specimens tested under the σ'_3 of 92 kPa, 196 kPa, 442 kPa and 1241 kPa, respectively, whereas the e_0 of 0.61, 0.61 and 0.59 are used for simulating dense specimens tested under the σ'_3 of 98 kPa, 294 kPa and 589 kPa, respectively. For undrained tests, the e_0 for simulating loose specimens are 0.87, 0.87, 0.86, and 0.85, corresponding to the σ'_3 of 98 kPa, 294 kPa, 490 kPa and 1069 kPa, respectively; whereas the e_0 of 0.63, 0.61, 0.59 and 0.59 are used for simulating dense specimens tested under the σ'_3 of 98 kPa, 1030 kPa, 1481 kPa and 1982 kPa, respectively. It is shown in Fig. 14 that the model simulates well the drained stress–strain behaviours of Sacramento River sand under both loose and dense states. Loose specimens exhibited strain hardening and volumetric contraction; however, a clear peak state followed by a decrease of the deviator stress and volumetric dilation can be observed in dense specimens. These key features of the drained response of Sacramento River sand can be appropriately captured by the α-plasticity model. Figure 15 shows the observed and

predicted undrained behaviour of loose Sacramento River sand, where a good agreement between the model predictions and test results can be observed. All the specimens are predicted to finally reach the critical-state flow, which match well with the experimental observations. Figure 16 presents the model predictions of the undrained behaviour of dense Sacramento River sand. It is found that the predicted deviator stress increased continuously with the increase of axial strain, which agrees well with the corresponding test results. Besides, with the increase of axial strain, the mean effective principal stress of specimens subjected to σ'_3 of 1030 kPa, 1481 kPa and 1982 kPa initially decreased and then increased towards steady-state flow. These features can be all reasonably depicted by the proposed model. Note that the test data after 10% strain cannot be provided here, because the original data in [27] were not given.

6 Discussions on model limitations

Even though the developed approach has positive performances when simulating the stress and strain behaviour of different sands, it could have several limitations that are associated with the type of critical-state line. Discussions will be thus made in terms of the critical-state lines that are usually used in engineering practice. It is easy to summarise the following three typical critical-state lines: (1) linear representation of the critical-state line in the $e - \ln p'$ plane, (2) linear representation in the $e - (p'/p_a)^\xi$ plane and (3) nonlinear representation in the $e - \ln p'$ plane.

If the first type of critical-state line was used, then the established model would not be able to characterise the constitutive behaviour of sand with wide initial material states, by only using one set of model parameters. This is due to the significant particle breakage of sand that can shift the critical-state points downwards [32, 79], which would inevitably change the critical-state parameters in the $e - \ln p'$ plane. This type of critical-state line can be used for modelling the stress–strain response of soft soils, e.g., clay, but should be avoided in current study.

For unified modelling of the critical-state behaviour of sand with a wide range of initial material states, the linear critical-state line in the $e - (p'/p_a)^\xi$ plane can be used. However, this kind of critical-state line may also result in some limitations of the developed model. As can be observed in Fig. 2, if the material state was initially at point C, where the e_0 was quite large while p' was quite small, the calculated critical-state stress, p'_c, at undrained loading condition could be unreasonably negative. This could be also encountered in classical models [67, 69] using the state pressure index, I_p (p', p'_c). In this kind of

situation, $p'_c = 0$ could be probably assumed for conducting the subsequent numerical simulation. However, in practical engineering, for example, embankment and foundation engineering, this kind of density and pressure conditions should be infrequently reached. Possible ground treatment technique would be applied to compact and consolidate the soil towards initial state point D, before large-scale geotechnical construction.

In addition to points C and D, if the material was initially at point E, where the e_0 was small while p' was extremely large, the calculated critical-state void ratio, e_c, at drained loading condition would be unreasonably negative. However, this limitation can be readily resolved by incorporating the dependence of I_p into hardening modulus, as suggested by Wang et al. [67]. It may be also remedied by using the third type of critical-state line, i.e., the nonlinear one, in the $e - \ln p'$ plane, such as the one with three segments [45, 46] and the one with inverted S-shape [10, 31].

This model in current form is also unable to capture the true three-dimensional behaviour of sand, due to the ignorance of the dependence of Lode's angle on the strength and dilatancy behaviour of sand. However, this limitation can be resolved by incorporating the effect of Lode's angle on the critical-state, peak-state and dilatancy formulae, which had been well defined and applied in practice [16, 23, 34] and thus not repeated here for simplicity. It can be also extended by using some specific three-dimensional methods, for example, the transformed stress method [73–75] and the characteristic stress method [35, 55]. As the emphasis of current study is not put on three-dimensional modelling of sand, this aspect will not be investigated. For more details on extending the α-plasticity approach to consider complex loading, one can refer to Sun and Sumelka [55] and Sun et al. [62]. In addition, not all the functions have analytical solution when performing fractional derivative. Therefore, only those yielding functions with power-law form, for example, the modified Cam-clay yielding function, have been adopted for model development. Nonetheless approximate solutions can be easily calculated also cf. Sumelka and Nowak [54]. Moreover, this approach did not consider the strength anisotropy and pure compressive hardening of soil; thus, it cannot simulate the stress–strain or consolidation behaviour of soils with inherent or induced anisotropy.

7 Conclusions

To capture the state-dependent stress–strain behaviour of sand with a wide range of initial densities and pressures, an improved fractional-order (α) plasticity model was

developed by using a modified yielding surface. Then, the model was validated against a series of drained and undrained triaxial test results of different sands. Discussions on several limitations of the proposed approach were also made. The main findings can be summarised as follows:

1. The model contained nine parameters for describing the plastic deformation and two parameters for describing the elastic deformation. All of the model parameters can be obtained from traditional triaxial test results.

2. The model can well capture the drained and undrained stress–strain behaviour of different sands with a wide range of initial states. The strain hardening/softening and volumetric dilation/contraction behaviour of sand under drained loading conditions can be well captured. In addition, compared with the previous fractional models, this model used a modified yielding surface, which made it capable of reasonably predicting the steady-state flow, liquefaction, quasi-steady-state flow and temporary peak behaviour of sand under undrained loading conditions.

3. Due to the typical forms of the critical-state line, the model may not be able to well capture the undrained behaviour of sand with initially significant large void ratio and small mean effective principal stress. It may also fail to capture the drained behaviour of sand with initially significant small void ratio and large mean effective principal stress. The effect of Lode's angle on the critical-state, peak-state and dilatancy behaviour of sand was also ignored in this study, which would make the model unable to simulate the three-dimensional behaviour of sand.

4. In addition, the above study was inspired by Sumelka [52]; however, these two approaches have distinct differences. As discussed in Sun and Sumelka [56], the model in [52] was developed by accounting for the effect of neighbouring stress point on the material point of interest, where the lower and higher stress terminals adopted in defining fractional derivative were collected from neighbouring material points. On the contrary, this study is proposed by considering the stress distance from the current state to the corresponding critical state of the material point of interest. All the model parameters were proposed based on laboratory observation.

Appendix

In order to derive Eq. (17), the following analytical solutions of the power-law functions, $(\sigma' - \sigma'_c)^\mu$ and $(\sigma'_c - \sigma')^\mu$, are needed:

$$_{\sigma'_c}D^\alpha_{\sigma'}(\sigma' - \sigma'_c)^\mu = \frac{\Gamma(1+\mu)}{\Gamma(1+\mu-\alpha)}(\sigma' - \sigma'_c)^{\mu-\alpha} \quad (25)$$

$$_{\sigma'}D^\alpha_{\sigma'_c}(\sigma'_c - \sigma')^\mu = \frac{\Gamma(1+\mu)}{\Gamma(1+\mu-\alpha)}(\sigma'_c - \sigma')^{\mu-\alpha} \quad (26)$$

where μ is the power index. Details for deriving Eqs. (25) and (26) can be found in [44] and thus not repeated here for simplicity. Accordingly, Eq. (14) with $\beta = 0$ should be rearranged as:

$$\begin{aligned} f &= (q - q_c)^2 + 2q_c(q - q_c) \\ &\quad + M_c^2(p' - p'_c)^2 + 2M_c^2 p'_c(p' - p'_c) \\ &\quad - M_c^2 p'_0(p' - p'_c) + q_c^2 + M_c^2 p'^2_c - M_c^2 p'_0 p'_c \end{aligned} \quad (27)$$

and

$$\begin{aligned} f &= (q_c - q)^2 - 2q_c(q_c - q) \\ &\quad + M_c^2(p'_c - p')^2 - 2M_c^2 p'_c(p'_c - p') \\ &\quad + M_c^2 p'_0(p'_c - p') + q_c^2 + M_c^2 p'^2_c - M_c^2 p'_0 p'_c \end{aligned} \quad (28)$$

Then, substituting Eqs. (27) and (28) into Eqs. (25) and (26), respectively, one has:

$$\begin{aligned} d_g &= -\frac{_{p'}D^\alpha_{p'_c}f(p')}{_{q_c}D^\alpha_q f(q)} \\ &= M_c^2 \frac{(p' - p'_c) + (2-\alpha)(p'_c - p'_0/2)}{(q - q_c) + (2-\alpha)q_c}\left[\frac{p'_c - p'}{q - q_c}\right]^{1-\alpha} \end{aligned} \quad (29)$$

$$\begin{aligned} d_g &= -\frac{_{p'_c}D^\alpha_{p'}f(p')}{_q D^\alpha_{q_c}f(q)} \\ &= M_c^2 \frac{(p' - p'_c) + (2-\alpha)(p'_c - p'_0/2)}{(q - q_c) + (2-\alpha)q_c}\left[\frac{p' - p'_c}{q_c - q}\right]^{1-\alpha} \end{aligned} \quad (30)$$

Further substituting Eq. (2) into Eqs. (29) and (30), a unique stress–dilatancy equation is obtained:

$$d_g = M_c^{1+\alpha}\frac{(p' - p'_c) + (2-\alpha)(p'_c - p'_0/2)}{(q - q_c) + (2-\alpha)q_c}. \quad (31)$$

References

1. Agrawal OP (2007) Fractional variational calculus in terms of Riesz fractional derivatives. J Phys A Math Theor 40(24):6287–6303

2. Alipour MJ, Lashkari A (2018) Sand instability under constant shear drained stress path. Int J Solids Struct 150:66–82. https://doi.org/10.1016/j.ijsolstr.2018.06.003

3. Azizi A (2009) Experimental study and modeling behavior of granular materials in constant deviatoric stress loading. Amirkabir University of Technology, Iran

4. Bandini V, Coop MR (2011) The influence of particle breakage on the location of the critical state line of sands. Soils Found 51(4):591–600

5. Bardet JP (1986) Bounding surface plasticity model for sands. J Eng Mech 112(11):1198–1217. https://doi.org/10.1061/(ASCE)0733-9399(1986)112:11(1198)

6. Been K, Jefferies MG (1985) A state parameter for sands. Géotechnique 35(2):99–112. https://doi.org/10.1016/0148-9062(85)90263-3

7. Been K, Jefferies MG (2004) Stress dilatancy in very loose sand. Can Geotech J 41(5):972–989. https://doi.org/10.1139/t04-038

8. Caputo M (1967) Linear models of dissipation whose Q is almost frequency independent—II. Geophys J Int 13(5):529–539. https://doi.org/10.1111/j.1365-246X.1967.tb02303.x

9. Caputo M, Fabrizio M (2015) Damage and fatigue described by a fractional derivative model. J Comput Phys 293:400–408. https://doi.org/10.1016/j.jcp.2014.11.012

10. Cen WJ, Luo JR, Bauer E, Zhang WD (2018) Generalized plasticity model for sand with enhanced state parameters. J Eng Mech 144(12):04018108. https://doi.org/10.1061/(ASCE)EM.1943-7889.0001534

11. Choo J (2018) Mohr–Coulomb plasticity for sands incorporating density effects without parameter calibration. Int J Numer Anal Methods Geomech. https://doi.org/10.1002/nag.2851

12. Ciantia MO, Arroyo M, O'Sullivan C, Gens A, Liu T (2018) Grading evolution and critical state in a discrete numerical model of Fontainebleau sand. Géotechnique. https://doi.org/10.1680/jgeot.17.p.023

13. Dafalias YF, Manzari MT (2004) Simple plasticity sand model accounting for fabric change effects. J Eng Mech 130(6):622–634. https://doi.org/10.1061/(ASCE)0733-9399(2004)130:6(622)

14. Eslami MM, Pradel D, Brandenberg SJ (2018) Experimental mapping of elastoplastic surfaces for sand using undrained perturbations. Soils Found 58(1):160–171. https://doi.org/10.1016/j.sandf.2017.12.004

15. Feia S, Sulem J, Canou J, Ghabezloo S, Clain X (2014) Changes in permeability of sand during triaxial loading: effect of fine particles production. Acta Geotech 1:19. https://doi.org/10.1007/s11440-014-0351-y

16. Gajo A, Muir Wood D (1999) A kinematic hardening constitutive model for sands: the multiaxial formulation. Int J Numer Anal Methods Geomech 23(9):925–965. https://doi.org/10.1002/(SICI)1096-9853(19990810)23:9%3c925:AID-NAG19%3e3.0.CO;2-M

17. Gajo A, Muir Wood D (1999) SevernTrent sand: a kinematic-hardening constitutive model: the $q - p$ formulation. Géotechnique 49(5):595–614

18. Golchin A, Lashkari A (2014) A critical state sand model with elastic–plastic coupling. Int J Solids Struct 51(15):2807–2825. https://doi.org/10.1016/j.ijsolstr.2014.03.032

19. Heidarzadeh H, Oliaei M (2018) Development of a generalized model using a new plastic modulus based on bounding surface plasticity. Acta Geotech 13(4):925–941. https://doi.org/10.1007/s11440-017-0599-0

20. Ishihara K, Tatsuoka F, Yasuda S (1975) Undrained deformation and liquefaction of sand under cyclic stresses. Soils Found 15(1):29–44. https://doi.org/10.3208/sandf1972.15.29

21. Jin Y, Wu Z, Yin Z, Shen JS (2017) Estimation of critical state-related formula in advanced constitutive modeling of granular material. Acta Geotech 12(6):1329–1351. https://doi.org/10.1007/s11440-017-0586-5

22. Jocković S, Vukićević M (2017) Bounding surface model for overconsolidated clays with new state parameter formulation of hardening rule. Comput Geotech 83:16–29. https://doi.org/10.1016/j.compgeo.2016.10.013

23. Kan M, Taiebat H, Khalili N (2014) Simplified mapping rule for bounding surface simulation of complex loading paths in granular materials. Int J Geomech 14(2):239–253. https://doi.org/10.1061/(ASCE)GM.1943-5622.0000307

24. Kang X, Xia Z, Chen R, Ge L, Liu X (2019) The critical state and steady state of sand: a literature review. Mar Georesour Geotechnol 37:1–14

25. Khalili N, Habte MA, Valliappan S (2005) A bounding surface plasticity model for cyclic loading of granular soils. Int J Numer Methods Eng 63(14):1939–1960. https://doi.org/10.1002/nme.1351

26. Lade PV, Nelson RB, Ito YM (1987) Nonassociated flow and stability of granular materials. J Eng Mech 113(9):1302–1318. https://doi.org/10.1061/(ASCE)0733-9399(1987)113:9(1302)

27. Lee KL, Seed HB (1967) Drained strength characteristics of sands. J Soil Mech Found Div 93(6):117–141

28. Li X (2002) A sand model with state-dependent dilatancy. Géotechnique 52(3):173–186

29. Li X, Dafalias Y (2000) Dilatancy for cohesionless soils. Géotechnique 50(4):449–460. https://doi.org/10.1680/geot.2000.50.4.449

30. Li X, Wang Y (1998) Linear representation of steady-state line for sand. J Geotech Geoenviron Eng 124(12):1215–1217. https://doi.org/10.1061/(ASCE)1090-0241(1998)124:12(1215)

31. Liu M, Gao Y (2016) Constitutive modeling of coarse-grained materials incorporating the effect of particle breakage on critical state behavior in a framework of generalized plasticity. Int J Geomech 17(5):04016113. https://doi.org/10.1061/(ASCE)GM.1943-5622.0000759

32. Liu HB, Zou DG (2013) Associated generalized plasticity framework for modeling gravelly soils considering particle breakage. J Eng Mech 139(5):606–615. https://doi.org/10.1061/(ASCE)EM.1943-7889.0000513

33. Liu HB, Zou DG, Liu JM (2014) Constitutive modeling of dense gravelly soils subjected to cyclic loading. Int J Numer Anal Methods Geomech 38(14):1503–1518. https://doi.org/10.1002/nag.2269

34. Liu M, Zhang Y, Zhu H (2017) 3D elastoplastic model for crushable soils with explicit formulation of particle crushing. J Eng Mech 143(12):04017140. https://doi.org/10.1061/(ASCE)EM.1943-7889.0001361

35. Lu D, Liang J, Du X, Ma C, Gao Z (2019) Fractional elastoplastic constitutive model for soils based on a novel 3D fractional plastic flow rule. Comput Geotech 105:277–290. https://doi.org/10.1016/j.compgeo.2018.10.004

36. Lü X, Huang M, Andrade JE (2018) Modeling the static liquefaction of unsaturated sand containing gas bubbles. Soils Found 58(1):122–133. https://doi.org/10.1016/j.sandf.2017.11.008

37. McDowell G (2002) A simple non-associated flow model for sand. Granul Matter 4(2):65–69

38. McDowell G, de Bono JP (2013) On the micro mechanics of one-dimensional normal compression. Géotechnique 63(11):895–908

39. McDowell GR, Yue P, de Bono JP (2015) Micro mechanics of critical states for isotropically overconsolidated sand. Powder Technol 283:440–446. https://doi.org/10.1016/j.powtec.2015.05.043

40. Meghachou M (1992) Stabilitédes sables laches: essais et modélisations. Université d'Oran

41. Pastor M, Zienkiewicz OC, Chan AHC (1990) Generalized plasticity and the modelling of soil behaviour. Int J Numer Anal Methods Geomech 14(3):151–190. https://doi.org/10.1002/nag.1610140302

42. Pedroso DM, Sheng DC, Zhao JD (2009) The concept of reference curves for constitutive modeling in soil mechanics. Comput Geotech 36(1):149–165

43. Pestana JM, Whittle AJ (1995) Compression model for cohesionless soils. Géotechnique 45(4):611–631

44. Podlubny I (1998) Fractional differential equations: an introduction to fractional derivatives, fractional differential equations, to methods of their solution and some of their applications, vol 198. Mathematics in science and engineering. Academic Press, San Diego

45. Russell A, Khalili N (2002) Drained cavity expansion in sands exhibiting particle crushing. Int J Numer Anal Methods Geomech 26(4):323–340

46. Russell AR, Khalili N (2004) A bounding surface plasticity model for sands exhibiting particle crushing. Can Geotech J 41(6):1179–1192

47. Russell A, Khalili N (2006) A unified bounding surface plasticity model for unsaturated soils. Int J Numer Anal Methods Geomech 30(3):181–212

48. Schofield A, Wroth P (1968) Critical state soil mechanics. McGraw-Hill, New York

49. Shi XS, Herle I (2017) Numerical simulation of lumpy soils using a hypoplastic model. Acta Geotech 12(2):349–363. https://doi.org/10.1007/s11440-016-0447-7

50. Shi XS, Herle I, Muir Wood D (2017) A consolidation model for lumpy composite soils in open-pit mining. Géotechnique 68(3):189–204. https://doi.org/10.1680/jgeot.16.P.054

51. Shi XS, Herle I, Yin J (2018) Laboratory study of the shear strength and state boundary surface of a natural lumpy soil. J Geotech Geoenviron Eng 144(12):04018093. https://doi.org/10.1061/(ASCE)GT.1943-5606.0001987

52. Sumelka W (2014) Fractional viscoplasticity. Mech Res Commun 56:31–36. https://doi.org/10.1016/j.mechrescom.2013.11.005

53. Sumelka W, Nowak M (2016) Non-normality and induced plastic anisotropy under fractional plastic flow rule: a numerical study. Int J Numer Anal Methods Geomech 40(5):651–675. https://doi.org/10.1002/nag.2421

54. Sumelka W, Nowak M (2018) On a general numerical scheme for the fractional plastic flow rule. Mech Mater 116:120–129. https://doi.org/10.1016/j.mechmat.2017.02.005

55. Sun Y, Sumelka W (2019) State-dependent fractional plasticity model for the true triaxial behaviour of granular soil. Arch Mech 71(1):23–47. https://doi.org/10.24423/aom.3084

56. Sun Y, Sumelka W (2019) Fractional viscoplastic model for soils under compression. Acta Mech. https://doi.org/10.1007/s00707-019-02466-z

57. Sun Y, Xiao Y (2017) Fractional order plasticity model for granular soils subjected to monotonic triaxial compression. Int J Solids Struct 118–119:224–234. https://doi.org/10.1016/j.ijsolstr.2017.03.005

58. Sun Y, Indraratna B, Carter JP, Marchant T, Nimbalkar S (2017) Application of fractional calculus in modelling ballast deformation under cyclic loading. Comput Geotech 82:16–30. https://doi.org/10.1016/j.compgeo.2016.09.010

59. Sun Y, Gao Y, Zhu Q (2018) Fractional order plasticity modelling of state-dependent behaviour of granular soils without using plastic potential. Int J Plasticity 102:53–69. https://doi.org/10.1016/j.ijplas.2017.12.001

60. Sun Y, Chen C, Song S (2018) Generalized fractional flow rule and its modelling of the monotonic and cyclic behavior of granular soils. In: Zhou A, Tao J, Gu X, Hu L (eds) Proceedings of GeoShanghai 2018 international conference: fundamentals of soil behaviours, Singapore, 2018//2018. Springer, Singapore, pp 299–307

61. Sun Y, Gao Y, Shen Y (2019) Mathematical aspect of the state-dependent stress-dilatancy of granular soil under triaxial loading. Géotechnique 69(2):158–165. https://doi.org/10.1680/jgeot.17.t.029

62. Sun Y, Gao Y, Song S, Chen C (2019) Three-dimensional state-dependent fractional plasticity model for soils. Int J Geomech. https://doi.org/10.1061/(ASCE)GM.1943-5622.0001353

63. Taiebat M, Jeremić B, Dafalias YF, Kaynia AM, Cheng Z (2010) Propagation of seismic waves through liquefied soils. Soil Dyn Earthq Eng 30(4):236–257. https://doi.org/10.1016/j.soildyn.2009.11.003

64. Verdugo R, Ishihara K (1996) The steady state of sandy soils. Soils Found 36(2):81–91. https://doi.org/10.3208/sandf.36.2_81

65. Wan R, Guo P (1998) A simple constitutive model for granular soils: modified stress-dilatancy approach. Comput Geotech 22(2):109–133. https://doi.org/10.1016/s0266-352x(98)00004-4

66. Wan R, Nicot F, Darve F (2009) Micromechanical formulation of stress dilatancy as a flow rule in plasticity of granular materials. J Eng Mech 136(5):589–598. https://doi.org/10.1061/(ASCE)EM.1943-7889.0000105

67. Wang Z, Dafalias Y, Li X, Makdisi F (2002) State pressure index for modeling sand behavior. J Geotech Geoenviron Eng 128(6):511–519. https://doi.org/10.1061/(ASCE)1090-0241(2002)128:6(511)

68. Xiao Y, Liu H (2016) Elastoplastic constitutive model for rockfill materials considering particle breakage. Int J Geomech 17(1):04016041. https://doi.org/10.1061/(ASCE)GM.1943-5622.0000681

69. Xiao Y, Liu H, Chen Y, Jiang J (2014) Bounding surface plasticity model incorporating the state pressure index for rockfill materials. J Eng Mech 140(11):04014087. https://doi.org/10.1061/(ASCE)EM.1943-7889.0000802

70. Xiao Y, Liu H, Chen Y, Jiang J (2014) Bounding surface model for rockfill materials dependent on density and pressure under triaxial stress conditions. J Eng Mech 140(4):04014002. https://doi.org/10.1061/(ASCE)EM.1943-7889.0000702

71. Xiao Y, Sun Y, Yin F, Liu H, Xiang J (2017) Constitutive modeling for transparent granular soils. Int J Geomech 17(7):04016150. https://doi.org/10.1061/(ASCE)GM.1943-5622.0000857

72. Xiao Y, Sun Z, Stuedlein AW, Wang C, Wu Z, Zhang Z (2019) Bounding surface plasticity model for stress–strain and grain-crushing behaviors of rockfill materials. Geosci Front. https://doi.org/10.1016/j.gsf.2018.1010.1010

73. Yao Y, Wang N (2014) Transformed stress method for generalizing soil constitutive models. J Eng Mech 140(3):614–629. https://doi.org/10.1061/(ASCE)EM.1943-7889.0000685

74. Yao YP, Sun DA, Luo T (2004) A critical state model for sands dependent on stress and density. Int J Numer Anal Methods Geomech 28(4):323–337. https://doi.org/10.1002/nag.340

75. Yao YP, Hou W, Zhou AN (2009) UH model: three-dimensional unified hardening model for overconsolidated clays. Géotechnique 59(5):451–469. https://doi.org/10.1680/geot.2007.00029

76. Yao YP, Kong L, Zhou A, Yin J (2014) Time-dependent unified hardening model: three-dimensional elastoviscoplastic

constitutive model for clays. J Eng Mech 141(6):04014162. https://doi.org/10.1061/(ASCE)EM.1943-7889.0000885

77. Yao YP, Liu L, Luo T, Tian Y, Zhang JM (2019) Unified hardening (UH) model for clays and sands. Comput Geotech 110:326–343. https://doi.org/10.1016/j.compgeo.2019.02.024

78. Yin Z, Wu Z, Hicher P (2018) Modeling monotonic and cyclic behavior of granular materials by exponential constitutive function. J Eng Mech 144(4):04018014. https://doi.org/10.1061/(ASCE)EM.1943-7889.0001437

79. Yu F (2017) Particle breakage and the critical state of sands. Géotechnique 67(8):713–719. https://doi.org/10.1680/jgeot.15.P.250